

Highly-magnified multiply imaged Radio counterpart of the Sub-mm Starburst Emission in the Cluster-Lens MS0451.6–0305

A. Berciano Alba^{1,2}, M.A. Garrett¹, L.V.E. Koopmans² & O. Wucknitz¹

¹ Joint Institute for VLBI in Europe, Postbus 2, 7990 AA, Dwingeloo, The Netherlands

² Kapteyn Astronomical Institute, University of Groningen, P.O.box 800, 9700 AV, Groningen, The Netherlands

Received ...; accepted ...

Abstract. We present the 1.4 GHz map of the centre of MS0451.6–0305 and report the detection of gravitationally lensed radio emission, coincident with the previously discovered sub-mm lensed emission. The radio emission is resolved into 7 distinct components with predicted total magnifications $\mu > 10$, and the overall structure can be explained, using a simple lens model, with three multiply-imaged radio sources at $z \sim 2.9$. The morphology and scale of the radio and sub-mm emission are strikingly similar, extending $\sim 1'$ across the sky. This suggests that the radio and sub-mm emission both arise from the same sources, most likely high redshift star forming galaxies. One of the multiply-imaged radio sources is predicted to lie between the suggested optical/NIR counterparts in the source plane; together these sources constitute an interacting system extending across a region of ~ 10 kpc. Preliminary estimates of the total $S_{850\mu\text{m}}/S_{1.4\text{GHz}}$ flux density ratio appear to be consistent with the value expected from a SED similar to M82.

1. Introduction

Sub-mm galaxies (SMGs) were first detected by SCUBA¹ (Hughes et al. 1998) and are believed to be dusty star forming galaxies located at high redshift, $z > 2$ (Smail et al. 2002). Little is known about the objects associated with the faint end of the SMG population ($S_{850\mu\text{m}} < 2\text{mJy}$) but they are predicted to dominate (energetically) the population as a whole (Knudsen 2004). A recent statistical stacking analysis (Knudsen et al. 2005), suggests that distant red galaxies (DRGs) and Extremely Red Objects (EROs) contribute $\sim 50\%$ of the flux density of sub-mm sources with $0.5 < S_{850\mu\text{m}} < 5\text{mJy}$.

Intrinsically faint SMG cannot be easily detected, since their flux densities lie below the ~ 2 mJy confusion limit of SCUBA images at $850\mu\text{m}$. Typically they also fall well below the (thermally limited) sensitivity of current radio instruments, such as the VLA. Individual systems can often only be detected via strong gravitational lensing effects, produced by massive foreground clusters of galaxies (Knudsen 2004; Kneib et al. 2004; Garrett et al. 2005).

The spatial magnification provided by the lensing cluster overcomes instrumental confusion limitations in the sub-mm and also boosts the measured flux density of the source (provided the lensed images remain unresolved), thereby increasing the probability of detection (Blain 1997). Another advantage of cluster lensing, is that the magnification provided by the lens effectively increases the spatial resolution of the observations.

Send offprint requests to: berciano@astro.rug.nl

¹ Submillimetre Common-User Bolometer Array, mounted at the James Clerk Maxwell Telescope (JCMT)

The largest magnifications typically occur in cases of multiple imaging; in such cases the geometry of the image positions can also be used to accurately estimate the source redshift, assuming the cluster mass model is known or can be otherwise measured.

SMM J16359+6612, associated with the cluster Abell 2218, was the first intrinsically faint, multiply imaged SMG to be detected in both the sub-mm (Kneib et al. 2004) and radio (Garrett et al. 2005). In this paper, we present VLA 1.4 GHz radio observations of a second case, SMM J04542–0301 (Chapman et al. 2002a), associated with the cluster MS0451.6–0305.

MS0451.6–0305 is a cluster of galaxies situated at $z=0.55$ (Gioia & Luppino 1994) that has recently been studied using optical HST images and Near Infrared (NIR) data (Borys et al. 2004, hereafter B04). They conclude that the sub-mm emission is probably related to an interacting system of three objects lying at the same redshift ($z \sim 2.9$): a Lyman Break Galaxy (LBG) and a pair of Extremely Red Objects (EROs). In the optical and NIR images, the LBG is imaged into two visible arcs, and the ERO pair is the most probable explanation of five possibly lensed images (B04; Takata et al. 2003, hereafter T03). However, the emission coming from the north-eastern and the central regions of the sub-mm image cannot be reproduced only using the LBG and the ERO pair (see Fig.7 from B04).

In this paper, we present deep, high resolution 1.4 GHz VLA observations of SMM J04542–0301. Specifically, in Sect. 2, we describe the VLA data analysis and present the associated radio images. Section 3 describes a simple lens model for the system, in an attempt to explain the lensed nature of the radio

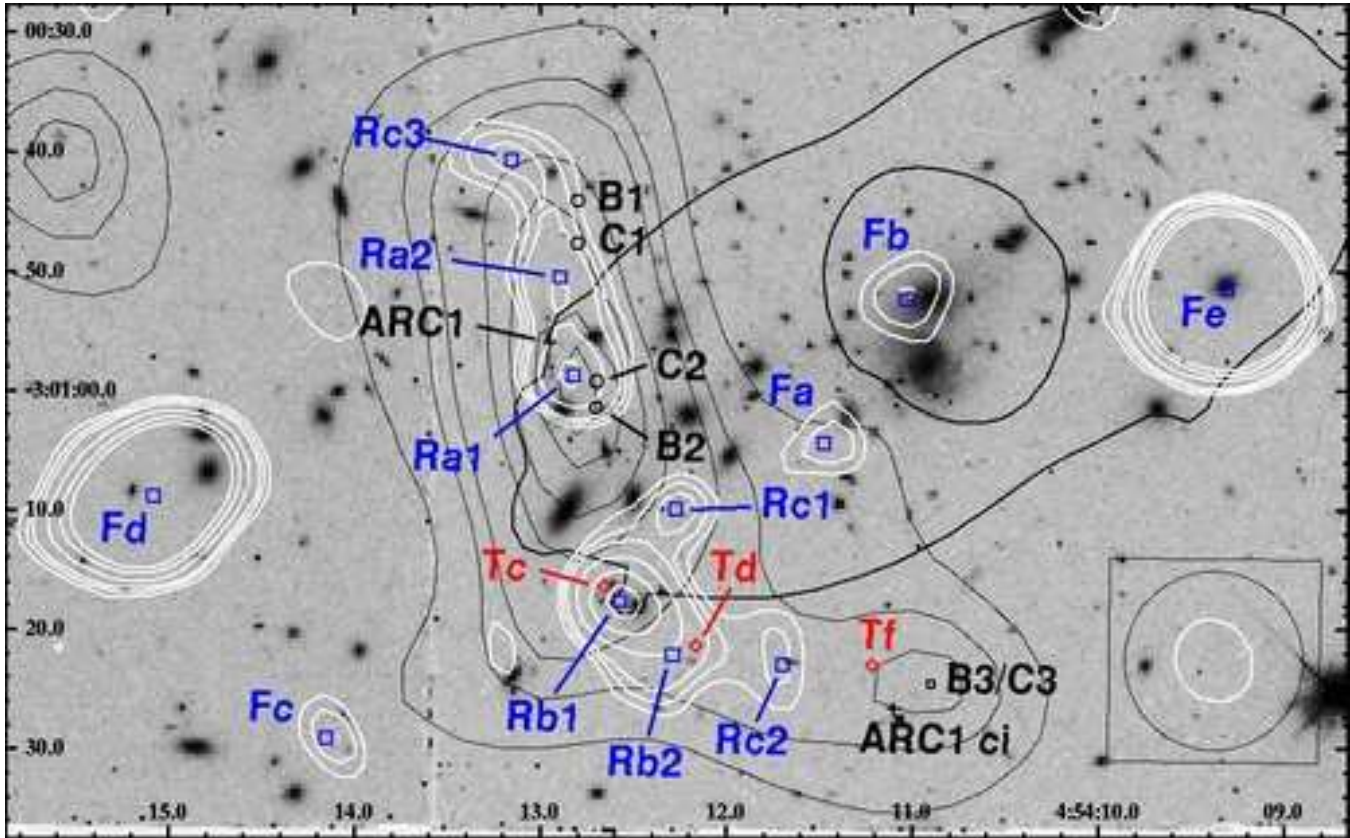


Fig. 1. The VLA 1.36 GHz naturally weighted contour map (solid white) superimposed upon the SCUBA 850- μ m contour map (solid black) and the inverted HST F702W image of the centre of the cluster MS0451.6–0305 (B04). The axis represent the right ascension (x-axis) and declination (y-axis) in the J2000 coordinate system. The solid thick black curve are the tangential (outer) and radial (inner) critical lines at $z=2.911$ from the lens model of the cluster used by B04. The blue boxes are the positions obtained trough a Gaussian fitting of the radio sources. The red diamonds are the positions of three EROs from (T03), and the black crosses/circles are the positions of a LBG lensed as two arc (ARC1 and ARC1 ci), and a triply-imaged EROs pair: B1/B2/B3 (images of ERO B) and C1/C2/C3 (images of ERO C) (see B04). The squares and circles have a size of 1'' to illustrate the systematic errors due to the alignment of the different images. Contours of the *radio map* are drawn at -3,3,4,5,8,12 & 16 times the $1-\sigma$ noise level of 9 μ Jy /beam. Contours of the *sub-mm map* are drawn at 4,6,7,9,10,11 & 11.5 mJy. The white circle inside a box in the bottom-left corner is the beam-size of the radio map (6.99×6.03 arcsec in position angle $PA = 32.59^\circ$)

emission related to SMM J04542–0301. In Sect. 4, we compare the radio and sub-mm emission, including a discussion about possible optical/NIR counterparts, and the preliminary calculation of the $S_{850\mu\text{m}}/S_{1.4\text{GHz}}$ flux density ratio. A summary and conclusions are presented in Sect. 5.

2. Radio Observations

VLA 1.4 GHz observations of the cluster MS0451.6–0305 were made on June 2002, and were retrieved from the NRAO data archive system². The integration time was 7.8 hours with the VLA in BnA configuration, employing two 25 MHz IFs in both left and right-hand circular polarisations. Each IF was subdivided into 7 channels each. The data analysis was performed using the NRAO AIPS package using standard analysis techniques. The absolute flux density scale was set by observations of 0137+331, and phase calibration was performed via short observations of 0503+020 between the 1 hour tar-

get scans. A wide-field image of the field was made and bright sources far from the field centre were subtracted from the data. Self-calibration using the remaining sources in the centre of the field realised images with a 1σ r.m.s. noise level of 9 μ Jy/beam.

In Fig.1, we present the radio contour map (solid white lines) of the naturally weighted VLA image of SMM J04542–0301, superimposed upon the HST F702W image and the sub-mm contour map (solid thin black lines) presented in B04. Note that the SCUBA beam is 15×15 arcsec, significantly poorer than the resolution of our radio map (6.99×6.03 arcsec). To compare the radio and sub-mm emission at the same resolution (see Sect. 4), we also produce a tapered image of the radio data, weighting down the long baselines to reach a Gaussian restoring beam similar to the SCUBA beam. The resulting map is presented in Fig.3 (solid white lines).

The AIPS task IMFIT was used to fit Gaussian components to all the radio sources detected in the field (3 and 4 Gaussians simultaneously, in the case of the two extended regions of radio emission in the naturally weighted map). The radio positions

² project ID AN0109, PI: Nakanishi

Table 1. Details of the radio sources associated with MS0451.6–0305. The columns show the position (RA, DEC), peak flux density (S_{Pk}), total flux density (S_T) and deconvolved Gaussian sizes (major axis, minor axis and position angle). In some cases the parameters of the Gaussian fits are not well constrained, these are indicated by a dash. The coordinates are shown as offsets with respect to the cluster centre, RA(J2000)=04:54:10.8 and DEC(J2000)=−03:00:51.6 (see T03, Table 2). A version of this table in absolute coordinates can be found in the online material.

Name	RA J2000 (")	DEC J2000 (")	S_{Pk} μJy	S_T μJy	Maj Axis (")	Min Axis (")	PA deg
Ra2	31.3±0.3	1.1 ± 0.4	70 ± 8	95 ± 18	6 ± 1	2 ± 1	27 ± 28
Ra1	30.3±0.2	−7.1 ± 0.2	109 ± 9	109 ± 9	—	—	—
Rb1	26.5±0.2	−26 ± 0.2	151 ± 9	151 ± 9	—	—	—
Rb2	22.3±0.5	−30.50 ± 0.7	52 ± 8	100 ± 22	9 ± 2	3 ± 2	158 ± 14
Rc1	22.1±0.6	−18.3 ± 0.4	50 ± 9	55 ± 16	6 ± 2	—	112 ± 11
Rc2	13.5±0.6	−31.3 ± 0.8	41 ± 8	58 ± 18	7 ± 2	1 ± 3	10 ± 163
Rc3	35.4±0.8	10.9 ± 0.5	52 ± 8	78 ± 19	8 ± 2	0 ± 2	73 ± 11
Fa	10.1±0.6	−12.7 ± 0.6	45 ± 9	50 ± 17	4 ± 6	0 ± 4	123 ± 38
Fb	3.5±0.6	−0.8 ± 0.6	49 ± 9	70 ± 20	6 ± 5	3 ± 6	122 ± 45
Fc	50.4±0.6	−37.5 ± 0.6	44 ± 9	44 ± 9	—	—	—
Fd	64.1±0.1	−17.2 ± 0.1	634 ± 9	1039 ± 21	7.6 ± 0.1	1.4 ± 0.5	128 ± 1
Fe	−22.40±0.02	−0.07 ± 0.02	1549 ± 9	1777 ± 17	3.3 ± 0.1	0.8 ± 0.5	125 ± 3

obtained are represented by square boxes in Fig.1. The results are listed in Table 1, together with their formal errors.

Radio source components *Ra*, *Rb*, *Rc* and *Fa* appear to be related to the sub-mm emission. The source *Fb* may be related to the central brightest cluster galaxy (BCG) (see Table 7), but there is no obvious NIR counterpart for *Fc*.

We also detect two bright radio sources, *Fd* and *Fe*. The latter is clearly identified with a optical/NIR counterpart, and both radio sources are almost two orders of magnitude brighter than the other radio sources in the field. These sources are probably not lensed images of the same background source — *Fe* is more compact than *Fd*, even though it is brighter. The positions of *Fd* and *Fe* are coincident (within the errors) with two radio sources already reported in Stocke et al. (1999) (see Table 7).

3. A lens model of the radio emission

In order to aid our interpretation of the radio emission associated with SMM J04542–0301, we have created a simple elliptical lens model plus external shear to describe the cluster lens potential. Our analysis employs the GRAVELENS software package developed by Keeton (2001). The modelling strategy is described in Sect.3.1, and the results of the model are discussed in Sect.3.2.

3.1. Modelling strategy

In Fig.1 we see that the tangential critical curve of the lens model used by B04 (black thick line) lies between the radio emissions *Ra1*–*Ra2*, *Rb1*–*Rb2* and *Rc1*–*Rc2*. Based on the general properties of lens geometry, this suggests that each of these image pairs belongs to a group of 3 images produced by one source close to the caustic in the source plane. Our working hypothesis to understand the lensing properties of the radio map is therefore as follows:

1. *Ra2*–*Ra1* are fold images of a source *Ra*, with an expected counterpart image (*Ra3*) close to *ARC1ci*.
2. *Rb1*–*Rb2* are fold images of a source *Rb* with an expected counterpart image (*Rb3*) close to *Rc3*.
3. *Rc1*–*Rc2*–*Rc3* are multiple images of a single source *Rc*, located behind the cluster.

To test this hypothesis, we used an NFW profile (Navarro et al. 1996) with (external) shear to model the overall mass distribution of the cluster, which was implemented with the GRAVELENS code (see the Appendix 1 for a more detailed description of the related formulae).

To constrain the model, we perform a number of distinct steps to fit the set of complex data that we have in hand. First, the parameters of the mass model are roughly chosen in order to reproduce the general shape of the critical lines determined by B04 (see Fig.1). Second, the positions and fluxes of the ERO images (*B1*, *C1*, *B2*, *C2*, *B3/C3*) are used as constraints for the first optimisation of the input model. And third, we included the positions and fluxes of the radio images as new constraints (following the previous hypothesis) to re-optimise the model. The constraints are listed in Tables 1 and 2. The coordinates of the cluster centre used in T03 were chosen as the origin of the coordinate system. Note that there might be systematic offsets between the different coordinate systems of order ~ 1 arcsecond which should be kept it in mind when we search for optical/infrared counterparts (see Sect.4.2).

3.2. Results

Figure 2 and Table 4 show the results of the lens model. Although the solutions are not unique, they are able to reproduce the positions of the EROs images and the radio emission *Ra1*, *Ra2*, *Rb1*, and *Rb2* very well. The largest offsets are found for *Rc1*, *Rc2* and *Rc3* (see panel 4 in Fig.2) which are the most distant images from the critical curves. This is consistent with

the effect of degeneracies of the global mass model near the critical curves: a change in the model parameters produces a more significant change in the image properties when they are further from the critical curves.

To improve the fit of images *Rc1-Rc2-Rc3*, the redshift of the model was changed for source *Rc*, but this only produces a radial shift of their predicted positions *in the same direction*, something that cannot improve the fit shown in panel 4. Therefore, we believe that the most important contribution to this offset is probably coming from the group of galaxies in the region between *Ra1* and *Rc1* (see Fig.1), which introduce perturbations in the overall mass distribution of the cluster not accounted for in the smooth NFW mass model.

One notable result is that the model predicts two faint counterpart images (*Ra3* and *Rb3*) that do not appear in our radio image. In our model *Ra3* and *Rb3* are less magnified than *Ra1-Ra2* and *Rb1-Rb2* respectively. The predicted relative magnifications suggest that *Ra3* and *Rb3* should appear in our maps at the 3 and 4 σ level respectively, but there is no evidence for this in the radio images. We note, however, that the predicted magnifications depend strongly on the overall mass model employed and perturbations by individual galaxies. They should be treated as rough estimates of the true magnification and the non-detection of these images suggests that this could be less than that predicted by these simple models.

The mass model parameters that characterise the NFW profile are summarised in Table 5. We note that the shear of the model is quite large, and the model centre is shifted $\Delta\text{RA}=-2.23''$ and $\Delta\text{DEC}=3.76''$ from the position of the assumed cluster's centre (although this is within the expected position errors). These effects are most likely systematic errors that compensate for the contribution of the group of galaxies that we are not including in the model, and the fact that we are forcing it to fit *Rb1* and *Rb2* as mirror images (a hypothesis that we will discuss in detail in Sect.4).

To check if our lens model is consistent with the gross properties of massive clusters of galaxies, we derive the concentration parameter, the virial mass and the virial radius of the cluster following the formalism presented in Bullock et al. (2001) (see Appendix 1 for details). The results are listed in table 3, together with the values obtained for the Coma cluster in Łokas & Mamon (2003). The only discrepancy between the

Table 2. Optical/NIR constraints used in the lens model. The columns show the position (RA, DEC), total flux density in K' band and predicted magnification μ (see also Table 1 in B04). The coordinates are shown as offsets with respect to the cluster centre, RA(J2000)=04:54:10.8 and DEC(J2000)=−03:00:51.6 (see T03, Table 2).

Name	RA J2000 (")	DEC J2000 (")	Flux in K' band μJy	μ
B1	29.95	7.498	3.6 ± 0.1	8 ± 1
B2	28.47	−9.702	1.9 ± 0.1	10 ± 1
C1	29.95	4	1.4 ± 0.1	10 ± 1
C2	28.47	−7.502	0.9 ± 0.1	5 ± 1
B3/C3	1.481	−32.9	2.5 ± 0.1	5 ± 1

values found for MS0451.6–0305 and the Coma Cluster comes from the concentration parameter, although we note that our value ($c_{\text{vir}} = 6.64$) is consistent within the 1σ confidence region around $c = 5$ predicted by the ACMD N-body simulations³. In addition, we note that Coma is at $z \sim 0$ and MS0451.6–0305 at $z=0.55$. Hence the concentration index of Coma should be larger (Bullock et al. 2001, see). Therefore, we conclude that the mass scale and scale radius of our lens model are consistent with the Coma cluster and ACMD simulations.

Table 3. Parameters of the cluster MS0451.6–0305 derived from the lens model: virial mass (M_{vir}), virial radius (R_{vir}) and concentration (c_{vir}). The details of their calculation are presented in Appendix A. The values for the Coma cluster were taken from Łokas & Mamon (2003)

Cluster	M_{vir}	R_{vir}	c_{vir}
MS0451.6-0305	$1.8 \times 10^{15} M_{\odot}$	2.6 Mpc	6.6
Coma	$1.2 \times 10^{15} M_{\odot}$	2.7 Mpc	9.4

It should be noted that our intention here is to only qualitatively show that the radio structure can arise from lensing, and not to present a detailed lens model of the cluster. With this idea in mind, we see that this simple mass model is able to reproduce the positions of the EROs and the radio images reasonably well, explaining the morphology of the radio map with three sources lying at $z=2.9$ in the source plane. In fact, the model predicts that the source *Ra* and the EROs *B* and *C* are located inside a region of about 1 arcsec in the source plane (see panel 6 of Fig.2), corresponding to a linear separation of 8 kpc⁴. The same situation is found in the case of the LBG and the ERO pair, which are separated by ~ 10 kpc in the source plane (see B04). This means that the radio source *Ra* is lying just between the LBG and the EROs, all of which are located in a region smaller than the extent of a typical galaxy (~ 20 kpc). It would appear therefore, that the radio source *Ra*, the LBG and the ERO pair indeed constitute an interacting or merging system of galaxies.

4. Comparison of the radio, sub-mm & optical/NIR data

In this section we make a more detailed comparison between our radio maps and the pre-existing sub-mm and NIR/optical (B04, T03) data.

4.1. Sub-mm vs Radio emission: morphology and flux density ratio

Figure 3 presents the sub-mm and tapered radio maps with a common resolution of $\sim 15'' \times 15''$. The regions of radio and sub-mm emission are not only coincident, but they are extended

³ extrapolation of the results obtained from lower mass haloes using the toy model developed in Bullock et al. (2001)

⁴ for a Λ CDM cosmological model with $\Omega_m=0.3$, $\Omega_\Lambda=0.7$ and $h_0=0.7$

Table 4. Lens model results. The columns show the coordinates of the predicted images (RA, DEC), predicted flux (S_T), offsets between the measured and predicted quantities (ΔRA , ΔDEC , S_T) and predicted magnification (μ). The coordinates are showed as offsets with respect to the cluster centre, RA(J2000)=04:54:10.8 and DEC(J2000)=−03:00:51.6 (see T03, table 2).

Name	RA (‘‘)	ΔRA (‘‘)	DEC (‘‘)	ΔDEC (‘‘)	S_T μJy	ΔS_T μJy	μ
B1	29.83	−0.12	7.26	0.24	3.03	0.54	5.23
B2	28.09	−0.38	−9.74	0.03	2.47	−0.60	4.26
B3	1.59	0.10	−32.59	−0.31	1.35	−0.11	2.32
C1	30.02	0.07	4.22	−0.22	1.40	0.02	7.38
C2	28.90	0.43	−7.44	−0.07	1.21	−0.31	6.34
C3	1.38	−0.10	−33.22	0.32	0.43	0.81	2.26
Ra2	31.13	−0.19	0.99	0.11	103.63	−8.63	10.27
Ra1	30.13	−0.12	−7.17	0.11	93.99	15.01	9.31
Ra3	3.18	−	−33.85	−	23.24	−	2.30
Rb1	26.71	0.19	−26.63	0.65	123.21	27.79	11.62
Rb2	21.96	−0.37	−30.56	0.06	117.18	−17.18	11.05
Rb3	38.24	−	2.34	−	38.06	−	3.59
Rc1	25.05	3.0	−21.37	3.11	65.95	−10.95	4.04
Rc2	12.45	−1.07	−30.26	−1.07	68.25	−10.25	4.18
Rc3	33.90	−1.45	11.34	−0.43	48.98	29.02	3

Table 5. Parameters of the NFW profile used to model the overall mass distribution of the cluster: Mass scale (κ_s), Galaxy position in arcsec (x_0 , y_0), ellipticity (e , θ_e), external shear (γ , θ_γ) and scale radius in arcsec (r_s).

Mass Model	κ_s	x_0	y_0	e	θ_e	γ	θ_γ	r_s
NFW	0.61	−2.23	3.76	0.63	−45.40	0.14	70.40	61.80

on the same angular scale ($\sim 1'$) and have a strikingly similar morphology. This strongly suggests that the radio and sub-mm emission are associated with each other and are produced by the same sources, probably star forming galaxies at $z > 2$ (Ivison et al. 2002; Smail et al. 2002; Chapman et al. 2003). In addition, the positions of the radio components located at $Rb1$, $Rb2$, $Rc1$, $Rc2$ and Fa (see Fig.1) are consistent with the sub-mm emission that could not be reproduced using only the ERO images and $ARC1$ (see B04, Fig.7).

However, Fig.3 also shows some differences in the morphology of the radio and sub-mm emission. The most obvious example is that the brightest region in sub-mm is not associated with the brightest region in radio ($Rb1/Rb2$), but with the second brightest one ($Ra1/Ra2$). One explanation for this apparent discrepancy in $Rb1/Rb2$, is that the radio and sub-mm emission arise from slightly different regions in the source plane and are differentially magnified. This effect could be quite significant for sources lying close to or extending across a caustic. Indeed, we note that recent Mid-IR and radio studies of local star forming galaxies show variations across the disk of up to a factor of ~ 5 in the ratio of the FIR and radio luminosity (Murphy et al. 2004). Another possibility is that the radio emission in the region $Rb1/Rb2$ is not only associated with the sub-mm emission that arises from high- z star formation but from an additional component, perhaps an AGN in the foreground cluster that has no counterpart in the sub-mm. Indeed, a galaxy cluster member

is located within $1.5''$ of the radio component $Rb1$, and may be a possible optical/NIR counterpart to this source (see table 7).

To make a simple estimate of the integrated flux density ratio $S_{850\mu\text{m}}/S_{1.4\text{GHz}}$ of the emission region, we used the AIPS task TVSTAT to integrate over the same area in the sub-mm and the tapered radio image. To be consistent, we used the 4 mJy/beam sub-mm contour shown in Fig. 1 and 3 to delimit the same integration area in both maps. Using this method, we find $S_{850\mu\text{m}} = 54.6 \pm 5.7$ mJy and $S_{1.4\text{GHz}} = 547.1 \pm 25.5$ mJy. The errors were calculated using the expresion $\sigma_{beam} \times \sqrt{N}$, where σ_{beam} is the noise per beam of the image, and N is the number of beams within the area delimited by the 4 mJy/beam sub-mm contour.

In addition, we used the redshifted SEDs of the archetypical star forming galaxies Arp220 and M82 (Polletta et al. in prep) to calculate the expected $S_{850\mu\text{m}}/S_{1.4\text{GHz}}$ flux density ratio in $MS0451.6 - 0305$, the faint sub-mm source detected in A2218 and the bright source detected in A1835 (see Table 6). We find that the measured ratio of the bright source in A1835 is closer to the expected value from the SED of Arp220, whereas in the case of the faint sources in A2218 and $MS0451.6 - 0305$, the measured ratio is closer to that expected with the SED of M82. However, we note that the measured ratio in $MS0451.6 - 0305$ may be underestimated if the relatively bright radio emission associated with $Rb1/Rb2$ arises from “radio-loud” AGN activity. In this case, a SED similar to Arp 220 may be more ap-

proprieate for this source. In any case, the overall flux density ratio is consistent with the favoured hypothesis that the bulk of the radio/sub-mm emission is arising from distant star forming galaxies.

Finally, we note that the tapered map (see Fig.3) shows an extension of the radio emission towards $B3/C3$ which is not seen in Fig.1. This suggests the possible existence of an extended radio source in this region, presumably associated with the faint sub-mm emission “toe” apparent in the image presented by B04.

4.2. Optical/NIR counterparts to the radio emission

B04 proposed that the sub-mm emission is related with three objects (see Fig.1): A LBG (imaged as $ARC1$ and $ARC1ci$) and a pair of triply-imaged EROs (B , imaged as $B1/B2/B3$; and C , imaged as $C1/C2/C3$).

As is shown in Fig.1, $ARC1$ is situated well inside the region of radio emission associated with $Ra1/Ra2$, and is therefore probably related to it. However, in the case of the ERO pair, the images $B1$ and $C1$ are located at the edge of the radio emission, suggesting that they are not directly contributing a significant amount of the radio flux density in this region. This is inconsistent with B04’s conclusions about the dominant contribution of the EROS pair ($\sim 2/3$) in the observed sub-mm flux (assuming that the radio and sub-mm emission are due to the same objects). Indeed, as shown in Fig.1, although $ARC1ci$ and TF (an ERO from T03) are most likely contributing to some of the measured flux density in the “sub-mm toe”, $B3/C3$ is coincident with the maximum of this region and is therefore a good NIR counterpart candidate to the sub-mm emission.

The offsets between the estimated centres of the radio emission and the optical/NIR candidates in the image plane are summarised in Table 7. Note that the offsets of $ARC1$ and the ERO images with respect to $Ra1$ and $Ra2$ are larger in declination ($\Delta DEC=3''$) than in right ascension ($\Delta RA=2''$). This is probably an effect of the magnification produced by the lens cluster — in this system the largest component of the magnification is preferentially aligned in the direction of declination (as is reflected in the direction of $ARC1$ and the overall morphology of the sub-mm and radio emission). Once we go to the source plane, our lens model predicts that the offset between Ra and the ERO pair in the image plane is reduced to $\sim 1''$. Indeed, as shown in Sect.3.2, the LBG and the EROs constitute an interacting system, with the radio source Ra expected to be situated between them in the source plane. This suggests that the detected radio and sub-mm emission may come from the region in which the systems interact, perhaps due to the enhanced star formation produced by the merging process. A similar phenomena is also observed in the Antennae galaxy, where the bulk of the $\lambda 20$ cm radio emission is situated between the nuclei of both galaxies (see Hummel & van der Hulst 1986). This scenario can also explain the inconsistency between the expected low contribution of the ERO pair in the radio emission and B04’s conclusions.

Moving to the southern region of Fig.1, the open diamonds correspond to the positions of three additional EROs reported

in T03. Two of these EROs (Tc and Td) are located within 2 arcseconds of $Rb1$ and $Rb2$ (see table 7), and may be their NIR counterparts. In this case we expect them to be mirror images, based on the predictions of our lens model. We note that T03 argue that these EROs have different photometric redshifts ($z_C = 3.730$, $z_D = 0.5$), which is inconsistent with that hypothesis. However, both show the same colours (within the errors) in all bands except for B and I_c , and in those cases the differences may be due to contamination effects (from the galaxy cluster members situated close to Tc) and the use of a different aperture in each source (see Takata et al. 2003, Table 1). Therefore, with this information we can not discard the possibility that Tc and Td are lensed images of the same source. On the other hand, the scenario in which Tc and Td are not mirror images (but still the optical/NIR counterparts of $Rb1$ and $Rb2$), is also possible within the lensing context. As is shown in Fig.1, $Rb1$ is located very close to the critical curve presented in B04, so a small change in its position can move it right on top of the critical curve (and the source component on top of the caustic) being therefore highly magnified. This is consistent with the non-detection of the predicted counterpart image $Rb3$, and the high brightness of $Rb1$ in the image plane. We also note that the shape of Tc is extremely elongated in the same direction of other faint arcs that appear in the same region of the Hubble image, suggesting that Tc may be lensed.

Another possibility (as discussed earlier in Sect.4), is that a foreground bright cluster galaxy member could be the NIR counterpart of $Rb1$. This other scenario can also explain the high brightness of $Rb1$ if the galaxy cluster member turns out to be a “radio loud” AGN.

Apart from the expected increase of the offsets due to the lensing magnification, we also identify four other possible sources of error. In order of importance these include:

- random measurement errors in the determination of the centre of the unresolved, blended radio components,
- errors in the choice of the position of $ARC1$, due to its extended and complicated structure,
- systematic errors due to differences between the HST and VLA coordinate reference systems (expected to be $\sim 1''$, but not dominant since no systematic trend is shown in Table 7).
- intrinsic offsets that can appear if the radio and sub-mm emissions come from different regions in the source plane.

Since we cannot properly estimate the contribution of these errors (with the exception of the systematic error), the offsets shown in Table 7 should be taken as indicative values.

5. Summary and Conclusions

We have presented deep VLA archive observations at 1.4 GHz of the centre of the cluster MS0451.6–0305, discovering a multiply-imaged radio counterpart of the sub-mm emission SMM J04542–0301 (B04), the second case of lensed radio emission coming from intrinsically faint SMGs (the first one is SMM J16359+6612 in A2218, see Kneib et al. 2004; Garrett et al. 2005).

Table 6. Flux density ratios. The columns show: name of the sub-mm emission (SMM), redshift at which the sub-mm source is expected to be after lensing (z), cluster in which is located the sub-mm emission (Cluster lens), flux density ratio obtained from observations (FDR observed), flux density ratios expected using the SEDs of Arp220 and M82 at redshift z (FDR Arp220, FDR M82), and percentage of deviation between the observed and expected flux density ratios (deviation obs-Arp220(%), deviation obs-M82(%)). The value of *FDR observed* in SMM J16359+6612 was calculated adding the fluxes of all the images together. The deviations were calculated as the difference between the observed and estimated ratios, divided by the bigger ratio between both of them.

SMM	z	Lens Cluster	FDR observed	FDR Arp220	deviation obs-Arp220(%)	FR M82	deviation obs-M82(%)	References
J14011+0252	2.56	A1835	127 ± 37	151	16	89	30	I01
J16359+6612	2.516	A2218	62 ± 10	145	57	85	28	K04; G05
J04542-0301	2.9	MS0451.6-0305	100 ± 11	201	62	114	34	Sect. 4.1

Table 7. Suggested NIR counterpart sources of some radio emissions. The columns show: name of the radio source (Radio Source), name of the suggested NIR counterpart (Counterpart Source), coordinates of the counterpart source (RA cs, DEC cs), Radio-NIR offsets (Δ RA, Δ DEC) and references that contain information about the counterpart sources (References). The coordinates are shown as offsets with respect to the cluster centre, RA(J2000)=04:54:10.8 and DEC(J2000)=−03:00:51.6 (see T03, Table 2). Note that the offsets presented in this table should be interpreted as indicative values (see Sect. 4.2 for details). A version of this table in absolute coordinates can be found in the online material.

Radio Source	Counterpart Source	RA cs (")	DEC cs (")	Δ RA (")	Δ DEC (")	References
Fb	BCG	1.1	−0.8	2.4	0.0	Stocke et al. (1999)
Fd	0451-03C	63.4	−16.2	0.8	1	Stocke et al. (1999)
Fe	0451-03A	−21.6	−1.2	0.7	1.1	Stocke et al. (1999)
Ra1	ARC1 centre	32.2	−4.3	1.9	−2.8	Borys, private communication
Ra1	ARC1 bottom end	31.9	−6.3	1.6	−0.8	Borys et al. (2004), F720W HST image
Ra2	ARC1 centre	32.2	−4.3	0.8	−3.2	Borys, private communication
Ra2	ARC1 top end	32.3	−1.7	0.9	2.8	Borys et al. (2004), F720W HST image
Ra2	B1	29.8	−0.1	−1.4	−6.4	Borys et al. (2004)
Ra2	C1	30.0	0.1	−1.4	−2.9	Borys et al. (2004)
Ra1	B2	28.5	−9.7	−1.8	2.1	Borys et al. (2004)
Ra1	C2	28.5	−7.5	−1.8	0.4	Borys et al. (2004)
Rb1	Tc	27.9	−24.7	1.4	−1.3	Takata et al. (2003)
Rb1	galaxy cluster member	24.8	−25.4	−1.8	−0.6	Borys et al. (2004), F720W HST image
Rb2	Td	20.5	−29.7	−1.8	−0.8	Takata et al. (2003)

With a resolution of 7×6 arcseconds, the radio emission can best be represented by seven discrete Gaussian components. A simple lens model of this system (based on a NFW mass profile) can reproduce the positions of the radio components assuming that they are multiple images of 3 sources located at $z=2.9$. However, the model raises some questions that need to be resolved (see Sect. 3.2).

The radio and sub-mm emission are clearly coincident, and exhibit a strikingly similar angular extension ($\sim 1'$) and shape. In addition, the flux density ratio ($S_{850\mu\text{m}}/S_{1.4\text{GHz}}$) calculated over the entire extent of the sub-mm and tapered radio emission, is consistent with the expected ratio derived from the redshifted SED of M82. These results suggest that the radio and sub-mm emissions are related to the same source/sources (star forming galaxies located at high redshift).

On the other hand, the radio and sub-mm emission also show some differences: the brightest peak of the radio emis-

sion is not coincident with the peak in the sub-mm. We find two possible scenarios that might explain the brightest peak (*Rb1*) in the radio map:

- the discrepancy in the sub-mm/radio morphology is due to differential magnification produced by the gravitational lensing effect – provided that the radio and sub-mm emissions arise from different regions of the galaxy. Indeed, *Rb1* is situated very close to the B04's critical curve.
- the observed radio flux in that region has an AGN component. This is consistent with one of the possible NIR counterparts of *Rb1*, a (foreground) galaxy cluster member that may host a “radio-loud” AGN.

The other possible optical/NIR counterpart of *Rb1* is an arc-shaped ERO (Tc), supporting the idea that *Rb1* might be lensed. Moreover, *Rb2* seems to be related with another ERO (Td) which shows similar colours as Tc. This, including the results of the lens model, supports the idea that *Rb1* and *Rb2* are images of the same source. However, this latter scenario

implies that the photometric redshifts of T_c and T_d obtained in T03 might be wrong. Unfortunately, none of the evidence is compelling enough to decide between the various scenarios that might explain the nature of $Rb1$ and $Rb2$ (see Sect. 4.2).

In the image plane, the association of the EROs mentioned in B04 with the radio emission appears to be somewhat uncertain — they are clearly located at the very edge of the radio emission. Assuming that the radio and sub-mm emission are due to the same sources, this result is inconsistent with B04's conclusions that the ERO pair contribute $\sim 2/3$ of the total sub-mm emission. When we look at the emission in the source plane, our model predicts that the radio source Ra is situated between the LBG and the ERO pair. All of these sources are located within a region spanning only ~ 10 kpc, strongly suggesting that they are physically related and constitute an interacting system (see also B04). Our interpretation of this result is that the interacting region of such a system might be the source of the radio and sub-mm emission (due to the intense star formation generated during the merging process), whereas the optical/NIR emission might correspond to the cores of the merging galaxies (a situation already observed e.g. in the Antennae galaxy). This scenario can explain the inconsistency of the results in radio and sub-mm with respect to the contribution of the ERO pair to the flux of the system. Note also that, although the common nature of SMGs and LBGs is unclear (Chapman et al. 2002b; Adelberger et al. 1998; Webb 2002), this framework allows us to relate the LBGs with SMMJ0452–0301 in a natural and consistent way via a merging process.

Further progress with this system requires an additional comparison of multi-wavelength data to be made and a more detailed lens model analysis to be performed. Deep, mid-IR observations, as well as higher resolution sub-mm data, might be very important in understanding this system, in particular to confirm the possible lensed nature of $Rb1$ and $Rb2$. We have recently re-observed MS0451.6–0305 using the VLA at 1.4 GHz in its most extended A-array configuration. These deeper and higher resolution observations may shed new light on some of the more controversial aspects raised in this paper. In particular, we aim to use the higher resolution VLA observations to securely identify possible optical and NIR counterparts, and try to resolve the radio images individually and determine their positions more accurately. In addition, we will attempt to take advantage of the large magnifications that may be associated with the brighter radio images, reconstructing the detailed radio structure of the background sources with unprecedented resolution using LENSCLEAN techniques (Wucknitz 2004).

Acknowledgements. The authors would like to thank Dr. Colin Borys for answering questions related with B04 and provide us with the lens model contours shown in B04, and the HST and SCUBA reduced images to prepare our figures. We also want to thank Dr. Charles Keeton who helped to solve problems with the GRAVELENS code during the modeling process, Dr. Andy Biggs for his assistance during the data reduction, Antonio Hernán Caballero for provide us the SED templates of Arp220 and M82, and Dr. John Stockes for answer questions related with the bright sources. ABA is also grateful

to A.F. Loenen for very valuable comments, suggestions and help during the writing of the manuscript. This work was supported by the European Community's Sixth Framework Marie Curie Research Training Network Programme, Contract No. MRTN-CT-2004-505183 "ANGLES".

References

Adelberger, K. L., Steidel, C. C., Giavalisco, M., et al. 1998, *ApJ*, 505, 18
 Blain, A. W. 1997, *MNRAS*, 290, 553
 Borys, C., Chapman, S., Donahue, M., et al. 2004, *MNRAS*, 352, 759, (B04)
 Bryan, G. L. & Norman, M. L. 1998, *ApJ*, 495, 80
 Bullock, J. S., Kolatt, T. S., Sigad, Y., et al. 2001, *MNRAS*, 321, 559
 Chapman, S. C., Blain, A. W., Ivison, R. J., & Smail, I. R. 2003, *Nature*, 422, 695
 Chapman, S. C., Scott, D., Borys, C., & Fahlman, G. G. 2002a, *MNRAS*, 330, 92
 Chapman, S. C., Shapley, A., Steidel, C., & Windhorst, R. 2002b, *ApJ*, 572, L1
 Garrett, M. A., Knudsen, K. K., & van der Werf, P. P. 2005, *A&A*, 431, L21, (G05)
 Gioia, I. M. & Luppino, G. A. 1994, *ApJS*, 94, 583
 Hughes, D. H., Serjeant, S., Dunlop, J., et al. 1998, *Nature*, 394, 241
 Hummel, E. & van der Hulst, J. M. 1986, *A&A*, 155, 151
 Ivison, R. J., Greve, T. R., Smail, I., et al. 2002, *MNRAS*, 337, 1
 Keeton, C. R. 2001, ArXiv Astrophysics e-prints, (astro-ph/0102340)
 Kneib, J.-P., van der Werf, P. P., Kraiberg Knudsen, K., et al. 2004, *MNRAS*, 349, 1211
 Knudsen, K. K. 2004, Ph.D. Thesis, leiden University
 Knudsen, K. K., van der Werf, P., Franx, M., et al. 2005, *ApJ*, 632, L9
 Lokas, E. L. & Mamon, G. A. 2003, *MNRAS*, 343, 401
 Luppino, G. A., Gioia, I. M., Hammer, F., Le Fèvre, O., & Annis, J. A. 1999, *A&AS*, 136, 117, (L99)
 Murphy, E. J., Helou, G., Armus, L., et al. 2004, American Astronomical Society Meeting Abstracts, 205,
 Navarro, J. F., Frenk, C. S., & White, S. D. M. 1996, *ApJ*, 462, 563
 Smail, I., Ivison, R. J., Blain, A. W., & Kneib, J.-P. 2002, *MNRAS*, 331, 495
 Stocke, J. T., Perlman, E. S., Gioia, I. M., & Harvanek, M. 1999, *AJ*, 117, 1967
 Takata, T., Kashikawa, N., Nakanishi, K., et al. 2003, *PASJ*, 55, 789, (T03)
 Webb, T. M. A. 2002, Ph.D. Thesis
 Wucknitz, O. 2004, *MNRAS*, 349, 1

Appendix A: Calculation of the concentration parameter and the virial mass of the cluster

The NFW density profile (Navarro et al. 1996) is defined in the three-dimensional space as:

$$\rho(r) = \frac{\rho_s}{(r/r_s)(1+r/r_s)^2} \quad (\text{A.1})$$

where ρ_s is the characteristic density and r_s is the scale radius.

However the GRAVLENS code (Keeton 2001) works with the projected surface mass density of the NFW profile, which is given by:

$$\kappa(r) = 2\kappa_s \frac{1-\mathcal{F}}{x^2-1}; \quad \kappa_s = \rho_s r_s / \Sigma_{\text{crit}} \quad (\text{A.2})$$

where $x = r/r_s$, κ_s is the mass scale, and \mathcal{F} is defined as:

$$\mathcal{F}(x) = \begin{cases} \frac{1}{\sqrt{x^2-1}} \tan^{-1} \sqrt{x^2-1} & (x > 1) \\ \frac{1}{\sqrt{1-x^2}} \tanh^{-1} \sqrt{1-x^2} & (x < 1) \\ 1 & (x = 1) \end{cases}$$

Following the formalism used in Bullock et al. (2001), we define the scale radius as:

$$r_s = R_{\text{vir}}/c_{\text{vir}} \quad (\text{A.3})$$

where c_{vir} is the concentration parameter and R_{vir} is the virial radius.

Comparing the definitions of virial mass used in Navarro et al. (1996) (M_{200}) and Bullock et al. (2001) (M_{vir}), the characteristic density can be written as:

$$\rho_s = \rho_u(z) \delta_c \quad (\text{A.4})$$

where $\rho_u(z)$ is the universal density at redshift z , and δ_c is the characteristic overdensity, which is linked with c_{vir} by the following expression:

$$\delta_c = \frac{\Delta_{\text{vir}}(z)}{3} f(c_{\text{vir}})$$

$$f(c_{\text{vir}}) = \frac{c_{\text{vir}}^3}{\log(1+c_{\text{vir}}) - \frac{c_{\text{vir}}}{1+c_{\text{vir}}}}$$

The parameter $\Delta_{\text{vir}}(z)$ is called the virial overdensity, and can be approximated (Bryan & Norman 1998) by:

$$\Delta_{\text{vir}}(z) \simeq (18\pi^2 + 82x - 39x^2)/\Omega_m(z) - 1$$

$$x = \Omega_m(z) - 1$$

Combining eq. 1 to 4, and the expression of κ_s showed in eq. A.2, the concentration parameter can be calculated using the following expression:

$$f(c_{\text{vir}}) = \frac{3 \kappa_s \Sigma_{\text{crit}}}{\rho_u(z_{\text{cl}}) r_s \Delta_{\text{vir}}(z_{\text{cl}})} \quad (\text{A.5})$$

The terms κ_s and r_s are given by the lens model (see table 5). Using the estimated redshift of MS0451.6–0305 from Luppino et al. (1999) ($z_{\text{cl}}=0.55$), $\rho_u(z_{\text{cl}})$ was calculated scaling the value for $z=0$ given in Bu01 ($\rho_u(z=0) = 8.3 \times 10^{10} h^2 M_{\odot} \text{Mpc}^{-3}$). Finally, the value of $\Delta_{\text{vir}}(z_{\text{cl}})$ was derived from equation (A) using the cosmological parameters chosen in Bu01 ($\Omega_m=0.3$, $\Omega_{\Lambda}=0.7$ and $h=0.7$).

The graphical resolution of eq.A.5 produce the value of c_{vir} listed in table 3 for the cluster MS0451.6–0305.

Finally, knowing the value of c_{vir} , the virial mass of the cluster can then be estimated as:

$$M_{\text{vir}} = \frac{4\pi}{3} \Delta_{\text{vir}}(z_{\text{cl}}) \rho_u(z_{\text{cl}}) R_{\text{vir}}^3 \quad (\text{A.6})$$

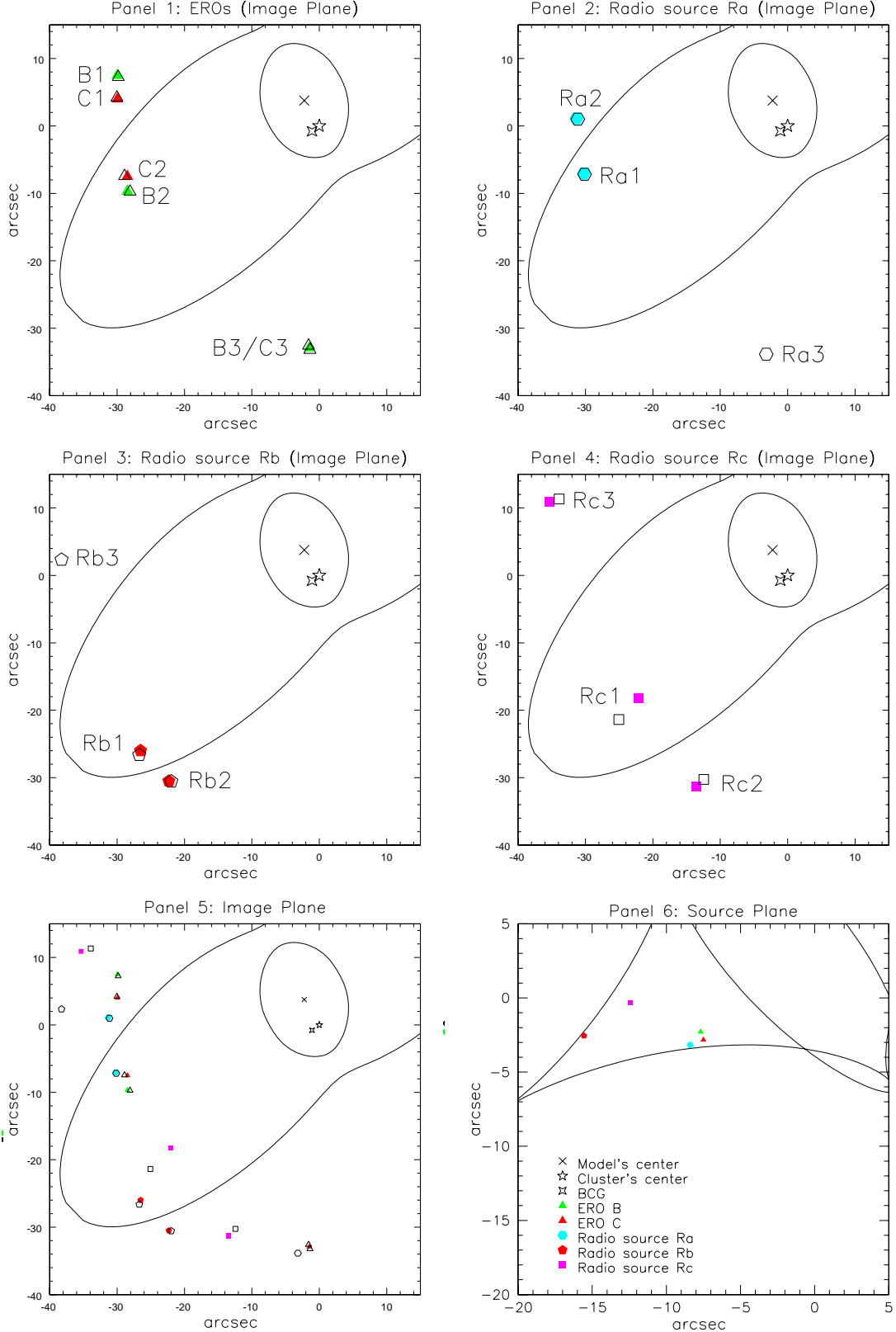


Fig. 2. Lens model results. The solid black curves represent the critical curves (image plane) and caustics (source plane) that define the model. Filled colour symbols represent the measured positions of the ERO images (B04) and the radio emissions, whereas empty black symbols are the predicted positions by the model. The EROs and each group of suggested multiple-imaged radio emissions are shown in different panels (1 to 4). Each colour relates one source in the source plane (panel 6) with the corresponding group of multiple-imaged radio emissions in the image plane. Coordinates of the centre of the lens model: RA(J2000)=04:54:10.8 and DEC(J2000)=−03:00:51.6 (see T03, table 2)

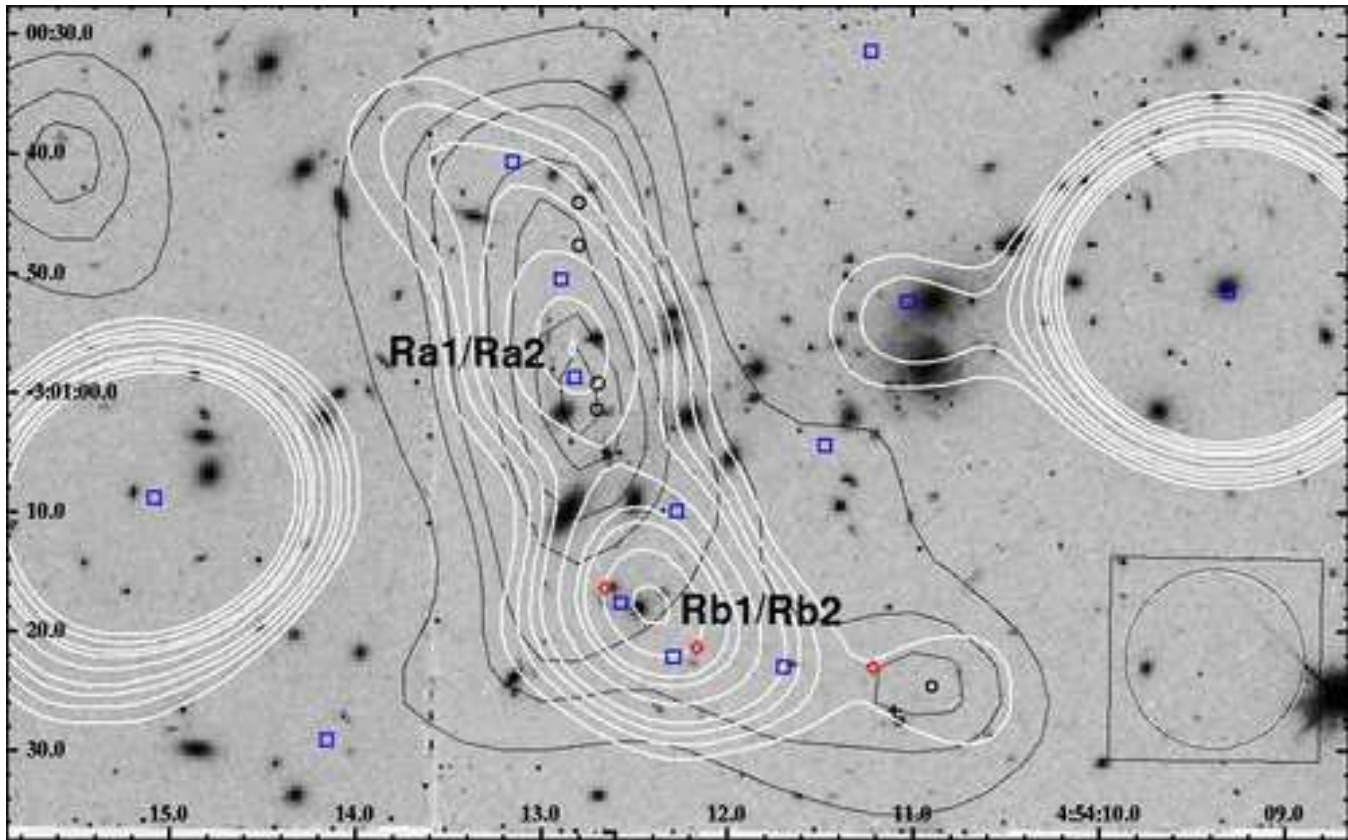


Fig. 3. The VLA 1.36 GHz tapered contour map (solid white) superimposed upon the SCUBA 850- μ m contour map (solid black) and the inverted HST F702W image of the centre of the cluster MS0451.6-0305 (B04). The axis represent the right ascension (x-axis) and declination (y-axis) in the J2000 coordinate system. Contours of the *tapered radio map* are drawn at -3,3,4,5,6,8,10,11,13 & 15 times the 1- σ noise level of 14.2 2 μ Jy/beam. Contours of the *sub-mm map* are drawn at 4,6,7,9,10,11 & 11.5 mJy. The positions of the radio sources and relevant objects in IR shown Fig.?? are plotted as reference points. The white circle inside a box in the bottom-left corner is the beam-size of the radio map (15.06 \times 14.26 arcsec, in position angle PA = 68.33°)